Journal of Membrane Science 636 (2021) 119539

Contents lists available at ScienceDirect

Journal of Membrane Science

journal homepage: www.elsevier.com/locate/memsci

High-efficient multifunctional electrochemical membrane for lithium polysulfide redox flow batteries

Tongshuai Wang [a], Xiaofeng Wang [b], Aaditya Pendse [a], Yuechen Gao [a], Kun Wang [a], Chulsung Bae [b,**], Sangil Kim [a,*]

[a] Department of Chemical Engineering, University of Illinois at Chicago, Chicago, IL, 60607, USA
[b] Department of Chemistry & Chemical Biology, Department of Chemical & Biological Engineering, Rensselaer Polytechnic Institute, Troy, NY, 12180, USA

ARTICLE INFO

Keywords:
Grid energy storage
Ion exchange membrane
Nanocomposite membrane
Lithium polysulfide redox flow battery
Capacity retention

ABSTRACT

Redox flow batteries (RFBs) based on lithium polysulfide (Li-PS) chemistry present great opportunities for large-scale energy storage and electric vehicles because of their use of abundant raw materials and their higher energy density compared with traditional flow batteries. However, to successfully implement Li-PS RFBs, issues related to the crossover of PS species through a membrane separator must be resolved. In this work, we demonstrate a facile method for fabricating a novel multifunctional electrochemical membrane (mECM) consisting of an organic ion exchange membrane reinforced with a porous carbon nanotube layer and a boron nitride layer. This rational design endows the membrane with remarkable ion selectivity and dimensional stability in organic electrolyte, leading to a greatly enhanced Li^+/PS ion selectivity, which exceeds that of a commercial polyolefin separator (i.e., Celgard 2325) by three orders of magnitude. A Li-PS RFB with the mECM exhibited stable electrochemical performance (0.05% capacity decay per cycle after 40 cycles) with 78% capacity retention over 100 cycles at 0.75C, while a reference cell with a Celgard 2325 membrane rapidly lost its capacity (0.33% capacity decay per cycle and 33% capacity at 100 cycles). Our results strongly suggest that the mECM with its high Li^+/PS ion selectivity is a promising membrane separator for developing high-performance Li-PS RFB systems.

1. Introduction

Reliable, low-cost energy storage systems with high energy capacity are crucial to meet expanding demands for large-scale smart grids and electric vehicles [1–3]. Among various energy storage systems, rechargeable lithium-ion-based batteries (LIBs) have received the most attention, as they are compact and environmentally friendly [4,5]. However, state-of-the-art LIBs cannot meet the requirements for large-grid-scale energy storage applications because of their relatively low capacity (<300 mAh g^{-1}), short lifetime (~10 years), and potential safety issues in confined systems (e.g., risk of fatal fire and explosion) [6]. Thus, considerable efforts have been dedicated to developing alternative new battery systems, such as aqueous vanadium redox flow batteries (VRFBs) [7,8]. Although VRFBs are widely employed for large-scale applications, such aqueous RFBs are limited by their extremely low energy density (10–20 mAh/g) and high vanadium costs [8–10].

In recent years, lithium-sulfur batteries (LSBs) have attracted growing interest because of their high theoretical energy density (2567 Wh kg^{-1}), high degree of environmental friendliness, use of naturally abundant raw materials, and low cost [11–13]. However, despite their compelling merits, the widespread employment of conventional LSBs for large-scale-grid applications has been hampered by several technical and economic limitations [14,15]: (1) a small cell cannot accurately reflect the electrochemical performance of a large cell because the LSB performance does not scale linearly with cell size; (2) complicated carbon/sulfur cathode synthesis procedures present challenges for generalization in large-scale manufacturing; (3) the actual battery capacity is limited due to low sulfur loading in a confined cell volume; (4) the scalability of the LSB is questionable because of slow reaction kinetics and ion transport for cases with higher sulfur loading and larger cell size [14]. In this regard, lithium polysulfide (Li-PS) RFBs, in which liquid Li_2S_8 catholyte replaces the solid sulfur cathode, have recently gained extensive attention for large-scale energy storage [16,17]. Li-PS RFB

* Corresponding author.
** Corresponding author.
E-mail addresses: baec@rpi.edu (C. Bae), sikim@uic.edu (S. Kim).

https://doi.org/10.1016/j.memsci.2021.119539
Received 22 March 2021; Received in revised form 8 June 2021; Accepted 15 June 2021
Available online 19 June 2021

systems integrate the high-capacity features of Li-PS chemistry and the general advantages of flow batteries, including a flexible system design, safer operation, and long cycle life [17,18], which can significantly mitigate the above-mentioned limitations of conventional static LSBs. Moreover, Li-PS RFBs can provide a higher energy density with much lower material costs than traditional aqueous flow batteries (e.g., all-vanadium flow batteries), due to the natural abundance of sulfur and lithium [17].

However, despite its great potential for a next-generation battery, the practical application of Li-PS chemistry to the development of high-performance RFBs has been hindered by the poor solubility of short PS chains in organic electrolytes and the crossover (i.e., shuttling) of intermediate PS species between the cathode and anode. PS shuttling can cause a rapid capacity decay, low coulombic efficiency, and undesired electrode fouling in lithium-sulfide or lithium-sulfur batteries [19–21], which presents a greater challenge in Li-PS RFBs due to the presence of highly concentrated PS in the electrolyte. To address these issues, one effective strategy is to employ a highly selective membrane separator that can suppress active PS species crossover while allowing rapid lithium-ion conducting [22–24]. Unfortunately, commercial porous battery separators (e.g., Celgard) cannot be adopted because PS ions are freely permeable through these membranes, which have pore sizes larger than PS molecules [25]. Thus, the use of non-porous ion exchange membranes (IEMs), which have been widely adopted in most aqueous RFBs (e.g., VRFBs) as ionic sieves, appears to be a more promising approach [26–29]. Nonetheless, conventional IEMs commonly show unsatisfactory performance in Li-PS batteries due to their poor dimensional stability in non-aqueous solvents (e.g., ether-based 1:1 mixture of dioxolane and dimethoxyethane), resulting in insufficient Li^+/PS^- selectivity and PS crossover through the membrane [30]. Therefore, there is a critical need for new membrane materials that are chemically/electrochemically compatible with Li-PS chemistry and capable of efficiently controlling Li^+ and PS transport to suppress PS shuttling during the operation of Li-PS RFBs.

In this study, we demonstrate a high-performance Li-PS RFB using a multifunctional nanocomposite electrochemical membrane (mECM) consisting of a chemical-resistant ion-exchange polymer, a porous carbon nanotube (CNT) layer, and a boron nitride nanotube (BNNT) membrane support. For the mECM matrix, we developed a novel lithiated biphenyl-based cation-exchange polymer (BPSA-Li) with outstanding Li^+/PS^- selectivity and excellent stability in organic electrolyte. The CNT layer can effectively reduce interfacial resistance and acts as a reinforcing material and additional PS barrier [31–33]. Meanwhile, the non-electrically-conductive BNNT layer facing the lithium anode facilitates heat dissipation and suppresses lithium dendrite growth [34]. This rational design enables the mECM to achieve almost complete rejection of PS species while maintaining a high ion selectivity and improving the electrochemical reaction kinetics between membrane and electrodes. A Li-PS RFB assembled with the mECM exhibits superior electrochemical performance, demonstrating its potential for grid-scale energy storage as well as a broad spectrum of other applications.

2. Experimental section

2.1. Reagents

Potassium thioacetate (KSAc, 98%, Sigma–Aldrich), dimethyl sulfoxide (DMSO, 99.9% Sigma–Aldrich), dimethylacetamide (99%, Honeywell), tetrahydrofuran (99.9%, Honeywell), methanol (99%, Fisher Chemical), acetone (99.5%, Fisher Chemical), DMSO-d_6, and $CDCl_3$ (99.96% D, Cambridge Isotope Laboratories) were purchased from the respective companies and used as received. 1,2-dimethoxyethane (DME), 1,3-dioxolane (DOL), and lithium bis(trifluoromethanesulfonyl)imide (LiTFSI) were purchased from Sigma–Aldrich and used without further purification. Lithium disulfide (Li_2S) and lithium metal foil were purchased from Fisher Scientific. Porous CNT layers were provided by Samsung, which were produced by a floating-catalyst-based chemical vapor deposition method [35]. BNNTs were purchased from BNNT, LLC. Polyvinylidene fluoride (PVDF) membranes with a pore size of 0.2 μm were purchased from Sterlitech.

2.2. BPSA synthesis

The details of our BPSA synthesis procedure can be found in our previous work [36–38]. In brief, BPSA (cation exchange polymer) was prepared by oxidizing the biphenyl thioacetate (BPTA) precursor, as illustrated in Fig. S1. BPTA polymer was synthesized via a nucleophilic substitution reaction of potassium thioacetate and a bromoalkyl-tethered precursor (BPBr-100). After the polymer was synthesized, a BPTA film was cast in a glass mold and subsequently immersed in a hydrogen peroxide solution to convert into BPSA via oxidation. The successful conversion of $–SC(=O)CH_3$ in BPTA to $–SO_3H$ in BPSA was confirmed by titrated ion exchange capacity measurements (2.29 meq./g) and FT-IR spectroscopy [36].

2.3. Membrane fabrication

The mECM fabrication procedure is shown in Fig. 1a. To prevent the formation of any excess cation exchange membrane (CEM) layers on the surface of the composite membranes during the BPSA infiltration procedure, a CNT membrane wetted with isopropyl alcohol (IPA) was placed on a Teflon plate and dried overnight. Then, the BPTA precursor was infiltrated into the CNT layer, and the BPTA/CNT composite was dried under vacuum to remove any entrapped air bubbles in the matrix. The porous BNNT layer was prepared by a typical nanotube buckypaper synthesis method. In brief, 5 mg of BNNTs was dispersed in 20 mL of IPA using ultrasonication. Afterward, the BNNT suspension was filtered under vacuum through the PVDF membrane. The prepared BNNT layer was attached to the BPTA/CNT composite using 5% BPTA/NMP solution as a glue. After the heterogeneous oxidation conversion of BPTA to BPSA, which was performed using 6 M formic acid and 30% H_2O_2 solution, the BPSA polymer was lithiated by immersion in 1.0 M LiOH solution at 80 °C for 12 h under stirring. The lithiated mECM was then rinsed with deionized water several times to remove any remaining salts and solvents. The prepared mECM was dried at 60 °C under vacuum and stored in an argon-filled glove box for ion transport evaluation and battery cell assembly.

2.4. Characterization of mECM

The CNTs and BNNTs used in the fabrication of the mECM were characterized by confocal Raman spectrometry (Raman-AFM, WITec alpha 300 RA) with an excitation wavelength of 532 nm (Nd:YAG laser). The morphology of the mECM was characterized by field emission scanning electron microscopy (FESEM, Hitachi S4800) and atomic force microscopy (TT-2 AFM, AFM Workshop) in tapping mode. The mechanical properties of the prepared mECM and reference samples (BPSA, Nafion, Celgard) were tested by a dynamic mechanical analyzer (TA Instruments, USA) and stress–strain curves of the membrane samples were measured at room temperature.

2.5. Solvent uptake, swelling ratio, and PS permeation test

To determine the effect of organic electrolyte on the PS anion diffusivity and chemical stability of the mECM, we examined the electrolyte uptake, swelling ratio (dimensional stability), and PS permeability of the mECM. The details of the test procedure can be found in our previous work [39,40]. After the membranes were equilibrated in an electrolyte solution with DOL/DME (1:1, v/v) and 1 M LiTFSI, the linear swelling (%) was determined by measuring the x, y, and diagonal lengths of dry and wet CEM samples. The electrolyte uptake (W_{elec} in wt.

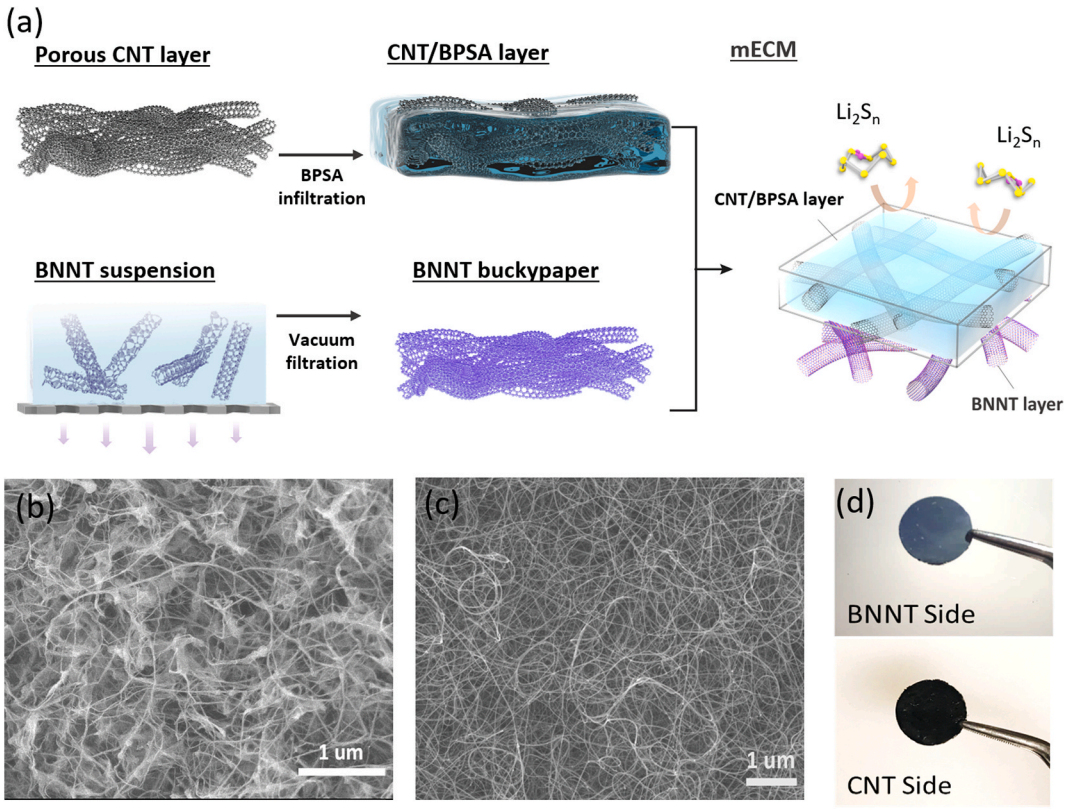

Fig. 1. (a) Schematic illustration of the mECM fabrication process. SEM images of (b) the BNNT layer and (c) CNT layer. (d) Photographs of the fabricated mECM: BNNT side (top) and CNT side (bottom).

%) values of the testing membranes were calculated by measuring the weights of wet *vs.* dry CEMs at room temperature according to

$$W_{Elec} = \frac{W_{wet} - W_{dry}}{W_{dry}} \times 100\% \quad (1)$$

The PS anion permeability across the membranes was measured using a side-by-side diffusion cell inside an argon-filled glovebox. The feed-side reservoir was initially filled with 0.1 M Li_2S_8 in DOL/DME (1:1, v/v) solution, and the permeant-side reservoir was filled with the same amount of DOL/DME (1:1, v/v) solution. The solution on each side was constantly stirred during the diffusion test to avoid concentration polarization. Ultraviolet–visible (UV–vis) spectroscopy was used to monitor the PS concentration in the permeant solution. The testing samples were carefully sealed in a UV quartz cuvette with a Teflon screw cap and were then quickly loaded in a UV chamber for testing. The PS concentration was determined from the change in absorbance signal. The PS permeability through the membrane was calculated from Fick's law:

$$V_B \frac{dC_B(t)}{dt} = A \frac{P}{L}(C_A - C_B(t)) \quad (2)$$

where V is the volume of the solution (mL), C_i is the PS concentration (mol/L), t is the test time (s), A is the active area (cm^2), P is the PS permeability (cm^2/s), and L is the membrane thickness (cm).

2.6. Li^+ ion conductivity measurement

The lithium-ion conductivity of the membranes was measured by electrochemical impedance spectroscopy (EIS). Prior to the measurement, the membrane samples were immersed in 1 M LiTFSI in DOL/DME (1:1, v/v) solution for 1 day. Then, the wet membrane was sandwiched between two stainless steel electrodes using a custom-designed Swagelok cell, as shown in Fig. S2a. Potentio-EIS was applied with a 50-mV AC bias scanning from 1 MHz to 10 Hz. The high-frequency x-axis intercept was taken to determine the membrane resistance. The membrane conductivity was then calculated using the following equation:

$$\sigma = \frac{L}{A \times R} \quad (3)$$

where σ is the conductivity (S/cm), L is the membrane thickness (cm), A is the active area (cm^2), and R is the membrane resistance (Ω).

2.7. Electrochemical characterization

The electrical conductivity of the CNT and BNNT buckypaper was measured using the four-probe method with a potentiostat (Autolab). The BNNT buckypapers were cut into strips and connected to copper wires using silver epoxy glue. The electrical current (DC) through the bulky paper strips was swept from 0 to 100 mA. The electrical resistance was obtained from the slope of the I–V curve, and the conductivity was calculated using Eq. 3.

Cyclic voltammetry (CV) curves of the Li-PS cells with different membranes were obtained on a potentiostat (Autolab) at a scan rate of 0.1 mV/s. The voltage window for the measurement was 1.4–3.5 V.

2.8. Li-PS stationary and flow cell test

The initial Li-PS battery performance of the mECM was evaluated using a nonflowing stationary Swagelok-type liquid cell before the Li-PS RFB was tested (Fig. S2a). In both the nonflowing Li-PS cell and the Li-PS RFB cell, lithium foil and Li-PS electrolyte were used as the anode and catholyte, respectively. All batteries were assembled in an argon-filled glove box. A 1 M Li_2S_8 catholyte solution was prepared by reacting stoichiometric amounts of Li_2S in electrolyte (DOL/DME v/v = 1:1) at 70 °C for 24 h [17]. A supporting electrolyte, 1 M LiTFSI, was added to the prepared catholyte solution to obtain a PS concentration of 0.1 M.

All membranes were soaked in the electrolyte solution for 1 day before each test. A voltage range of 1.8–2.8 V was used for the rate and cycle test in the nonflowing Li-PS cell. The active area for the nonflowing Li-PS cell was 0.712 cm^2. For the Li-PS RFB test, a customized semi-solid Li-PS RFB with an active membrane area of 1 × 2 cm^2 was used (Figs. S2b & S2c). The 7 mL of catholyte solution was circulated through the RFB cell using a peristaltic pump connected with Teflon tubing kits (Cole--Parmer) at a volumetric flow rate of 5 mL/min. A photograph of the RFB single cell is shown in Fig. S2c. The batteries were charged and discharged using an eight-channel battery analyzer (MTI Corporation), and the voltage range for cycling was controlled between 1.9 and 2.6 V.

3. Results and discussion

3.1. Membrane fabrication and characterization

Fig. 1a illustrates the fabrication method employed for the mECM. The mECM has two distinct layers, i.e., a CNT/BPSA layer and a BNNT layer with a thickness of ~5–10 μm, which are attached by using a very thin layer of BPSA as a glue (Fig. 1b). The porous CNT and BNNT layers used for the composite membrane fabrication were characterized by Raman spectroscopy and SEM. Fig. S3a indicates that the CNTs are well-graphitized with a G (1595 cm^{-1}) to D (1330 cm^{-1}) band ratio as high as 110 and a noticeable radial breathing mode, which suggests that a large population of CNTs is SWNTs and DWNTs. In addition to SEM, we also characterized our BNNT buckypaper using Raman spectroscopy. As shown in Fig. S3b, the Raman spectrum of the BNNT buckypaper shows a strong peak at 1366 cm^{-1}, which corresponds to the active E_{2g} tangential mode of BNNTs [41,42]. The Raman result indicates that the BNNT buckypaper is predominantly composed of high-quality BNNTs. The electrical conductivities of the individual CNT and BNNT buckypaper, as measured using the four-probe method, are shown in Table S1. Our porous CNT film has a high electrical conductivity of 55.96 S/cm, close to a previously reported value for CNT buckypaper [43], while the BNNT buckypaper has a much smaller conductivity of 0.135 S/cm due to the large bandgap in the electronic structure [44]. The insulating nature of the BNNT buckypaper is essential for our mECM fabrication, as it prevents a connection short between the CNT/BPSA layer and the lithium anode. In addition, as shown in Fig. S4 and Table S2, the mechanical strength of the mECM is significantly higher than that of other membrane samples. The calculated Young's modulus of mECM and pristine BPSA membrane are 1390 MPa and 760 MPa, respectively, which indicates the incorporation of the CNT film greatly improved the mechanical stabilities of the BPSA membrane. Meanwhile, Young's modulus values for Celgard and Nafion117 are 270 MPa and 187 MPa, respectively.

High-magnification SEM imaging and AFM analysis confirmed that the bundle size ranges from 20 to 30 nm and the visible pore size of the CNT buckypaper is approximately ~35 nm (Fig. S5). SEM images of the BNNT and CNT buckypapers, as shown in Fig. 1b and c, indicate that the nanotubes form a uniform pore structure with a high membrane surface porosity (>80%) due to the nanometer-sized bundles, which can ensure a high loading of ion exchange polymer (i.e., BPSA) into the CNT film. BNNT side and CNT side of the prepared mECM show a good uniformity without any visible structural defects (Fig. 1d).

We also characterized the morphology of the prepared mECMs via SEM and AFM. The SEM image of the CNT/BPSA layer shown in Fig. 2a indicates that the BPSA infiltrates well into the CNT layer without any defects or pinholes. A porous BNNT buckypaper was uniformly deposited on the backside of the CNT/BPSA layer, as shown in Fig. 2b. Unlike the CNT/BPSA side, in which BPSA is fully infiltrated into the CNT layer, the BNNT buckypaper was attached to the CNT/BPSA layer by using a thin BPSA layer as glue to minimize interfacial resistance from a thick CEM; therefore, the BNNT layer maintains the original morphology of the porous BNNT buckypaper. Moreover, we carefully removed the excess layer of BPSA on the CNT layer surface by using spin-coating to expose the highly electrically conductive CNTs, to obtain a smaller contact resistance between the mECM and the cathode electrode. As

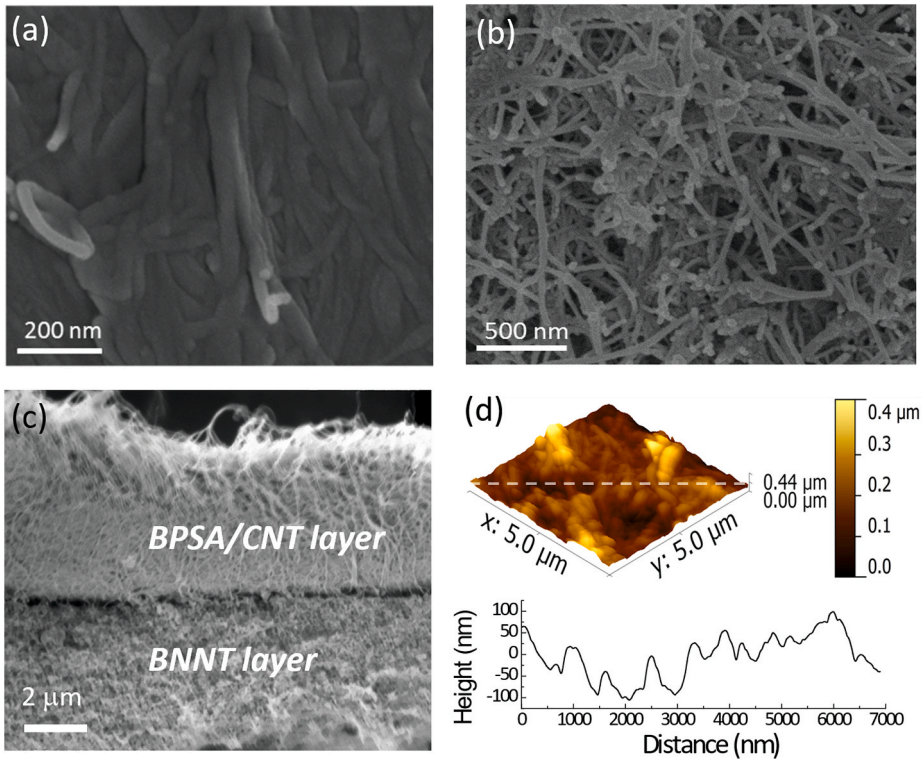

Fig. 2. SEM images of (a) the CNT/BPSA side of the mECM, (b) the BNNT side of the mECM, and (c) the cross-section of the mECM. (d) AFM image and height profile of the CNT/BPSA side of the mECM.

shown in Fig. 2c, cross-sectional SEM image of mECM indicates the two-layered structure of mECM consisting of BPSA/CNT layer and BNNT layer. AFM image clearly shows that the BPSA-coated CNT bundles are exposed (~0.44 μm) on the surface of the mECM without any excess BPSA layer (Fig. 2d). Thus, both SEM and AFM measurements confirmed the successful fabrication of the mECM.

3.2. Ion transport and electrochemical properties

Compared with the polyolefin-based porous battery separator (e.g., Celgard), most ion-exchange polymers show substantial swelling in non-aqueous Li-PS electrolyte, which inevitably leads to a high swelling ratio. A high swelling ratio can reduce the mechanical stability of the membrane and, more importantly, can increase the size of the ion/molecular transport channel, thus allowing larger PS molecules to migrate from the cathode to the anode side. Although BPSA is inherently stable in an organic solvent, we infiltrated BPSA into the highly entangled CNT matrix to minimize polymer swelling and to further enhance the ion selectivity of the mECM. The swelling ratio and solvent uptake (i.e., amount of absorbed solvent) of the mECM are compared with those of Nafion117, a pristine BPSA membrane, and Celgard 2325 in Fig. 3a. Because the swelling ratio is closely related to the solvent uptake, we use the swelling ratio of the CEMs (BPSA, Nafion, and mECM) to correlate their dimensional stability. Celgard 2325 does not show any swelling, ~0%, due to the inertness of polyolefin in organic solvents, and its porous structure exhibits a DOL/DME uptake of ~75%. In contrast, the Nafion membrane swells over 50%, with 57% solvent uptake in DOL/DME solution, indicating that Nafion is not suitable as a membrane separator for a Li-PS battery with DOL/DME electrolyte. The swelling ratio and solvent uptake values of the pristine BPSA membrane are 3% and 31%, respectively, which are much smaller than those of Nafion membranes. By combining BPSA with the CNT membrane, the swelling ratio of the mECM decreases to 1% because the robust, highly entangled CNT scaffold can suppress the swelling of BPSA. However, the mECM has a higher solvent uptake than the pristine BPSA membrane because the open pore structure of the BNNT membrane layer can hold more electrolyte than the dense structure of the BPSA membrane. The excellent dimensional stability and low swelling properties of BPSA in organic electrolyte require further study, and we are currently planning a systematic investigation of the BPSA molecular structure–stability relationship. For example, in future work, we will employ a suite of characterization tools (e.g., X-ray scattering, nuclear magnetic resonance, FT-IR) to quantitatively correlate the molecular structure of BPSA with its swelling properties in various organic solvents.

A low PS crossover through the separator is critical to suppress PS ion shuttling between two electrodes in order to ensure a low capacity loss and good cycle stability in Li-PS battery applications. To quantify the PS transport properties of the mECM in comparison to other reference membranes (Celgard 2325, Nafion, and BPSA membranes), the Li-PS diffusivity was measured for a side-by-side diffusion cell filled with 0.1 M Li_2S_8 in DOL/DME (1:1, v/v) solution on the retentate side and DOL/DME (1:1, v/v) solution on the permeate side. A magnetic stirrer was used in each side of the cell during the test to avoid concentration polarization. The test procedures are described in more detail in the experimental section. The calculated PS diffusivity values across the membranes are shown in Table S3. As shown in Fig. 3b and Table S3, the PS permeability (2.2×10^{-7} cm^2/s) of the Celgard 2325 membrane are the highest among all tested membrane separators, indicating rapid diffusion of PS molecules through the porous structures of the Celgard separator. In contrast, the CEM separators greatly suppressed the PS crossover during the test due to their dense matrix. The PS diffusivity of the BPSA-based membranes (i.e., pristine BPSA membrane and mECM) were lower than those of the lithiated Nafion membrane by two orders of magnitude (1.2×10^{-10} cm^2/s *vs.* 3.6×10^{-8} cm^2/s), which is similar to the trend observed for the swelling ratio and solvent uptake of the BPSA membrane. In particular, the mECM with BPSA infiltrated in the highly entangled CNT scaffold can effectively retain Li-PS molecules; thus, no Li-PS species passing through the mECM were detected by UV–Vis spectroscopy ($<1.0 \times 10^{-11}$ cm^2/s, PS detection limit) during the test, demonstrating the excellent PS-blocking ability of this membrane.

The electrochemical properties and lithium-ion conductivity of the membrane separators were characterized by EIS and CV measurements.

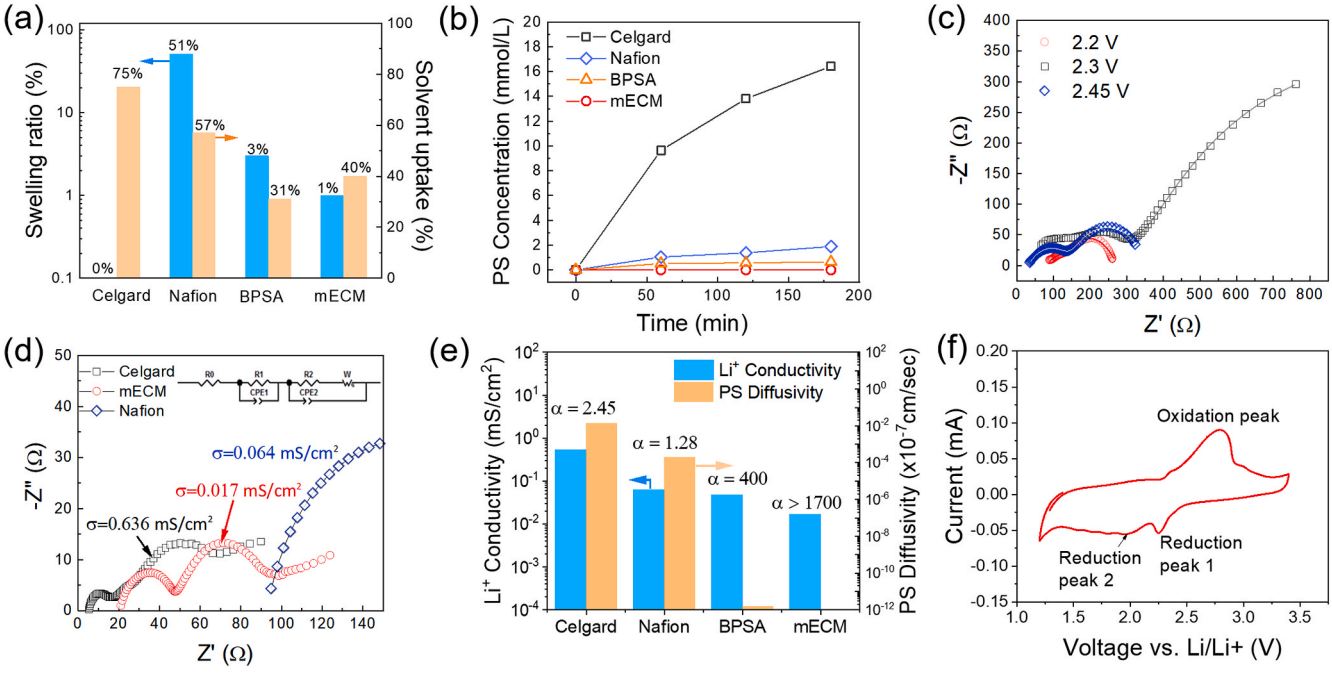

Fig. 3. (a) Swelling ratio and solvent uptake of Nafion 117, BPSA, mECM, and Celgard in electrolyte. (b) PS concentration vs. time during the PS diffusion measurement. (c) EIS curves of a Li-PS cell with the mECM, measured at different OCPs. (d) EIS curve of the Li-PS cell with Celgard, mECM, and Nafion. (e) Li^+ ion conductivity and PS diffusivity of Nafion, BPSA, mECM, and Celgard. Selectivity (α) is the ratio of Li^+ conductivity and PS diffusivity. (f) CV curve of a Li-PS cell with the mECM recorded at 0.1 mV/s.

We first investigated a Li-PS static cell with the mECM by performing EIS tests at different open-circuit voltages (OCVs). The impedance of the static cell is strongly dependent on the OCV (Fig. 3c), which is presumably due to the formation of insoluble PS compounds at different states of charge. Thus, we measured the battery impedance of different membranes at an OCP value of 2.45 V (Fig. 3d). To acquire detailed information on the battery impedance of the different membranes, Nyquist plots were fitted with an appropriate equivalent circuit. In this model, R_0 represents the membrane ionic resistance, R_{inter} is the interfacial resistance between the membrane and electrode, and R_{ct} is the charge transfer resistance. The through-plane conductivity of the membrane separator was calculated from the membrane ionic resistance obtained from the EIS spectra (Fig. 3d and Table S3). Among all the tested membranes, commercial Celgard 2325 membrane shows the lowest areal resistance (4.6 Ω) and the highest lithium ion conductivity (0.539 mS/cm) due to its highly porous structure that allows faster lithium ion transport. Compared to the porous Celgard 2325, Nafion and BPSA membranes exhibit much higher areal resistance due to their nm-size ionic channel size [36]. Although the lithium-ion conductivity through the pristine BPSA membrane (0.021 mS/cm) was lower than that of the lithiated Nafion (0.046 mS/cm), we were able to lower the membrane resistance of the BPSA membrane (86.5 Ω *vs.* 107.2 Ω) by decreasing the membrane thickness due to the good mechanical and chemical stability (low swelling ratio) of the BPSA membrane in organic solvent. Moreover, the thickness of the BPSA/CNT layer in the mECM can be reduced to 5 μm (total thickness of 15 μm for the mECM, including the 10-μm-thick porous BNNT layer) by reinforcing BPSA with a CNT membrane, which can further reduce the membrane resistance to 30.1 Ω. Fig. 3e shows the overall ion transport properties of the membranes tested in this study. The mECM demonstrates superior PS-blocking capability over the other membranes without a significantly decreased ionic conductivity, leading to the highest Li/PS selectivity among the tested membranes. It is worth noting that the Li/PS selectivity of the mECM is higher than that of Celgard and Nafion by at least three orders of magnitude. We also examined the battery chemistry of the mECM by conducting a CV test. The CV characteristics of the Li-PS static cell were assessed within a voltage window of 1.2–3.4 V *vs.* Li/Li^+ at a scan rate of 0.1 mV/s. As shown in Fig. 3f, an anodic (oxidation) peak at 2.78 V corresponding to the transition from Li-PS (Li_2S/Li_2S_2) to elementary sulfur can be clearly seen during the oxidation scan. Two cathodic (reduction) peaks, i.e., a higher reduction peak at 2.25 V and a relatively lower reduction peak at 1.97 V, are also visible, corresponding to the reduction of long chain PS to a shorter PS (Li_2S_n, $4 \leq n \leq 8$) and further reduction to Li_2S/Li_2S_2, respectively, as observed in other Li-PS battery studies [45].

3.3. Li-PS battery performance

Because the evaluation of membrane separators for Li-PS RFBs requires longer test times than that for typical rechargeable batteries (e.g., Li–S coin cells) due to the large volume of electrolytes and other operating parameters (e.g., flow rate, circulating electrolyte volume, cut-off voltage, electrolyte viscosity, and concentration), it is more reasonable to test the initial battery performance of the prepared mECMs using a nonflowing static liquid cell. Therefore, we used Swagelok-type static cells with a 0.3-mL loading of electrolyte to evaluate the initial Li-PS performance of the membranes (Fig. S2a).

We first evaluated the battery rate performance of mECM and

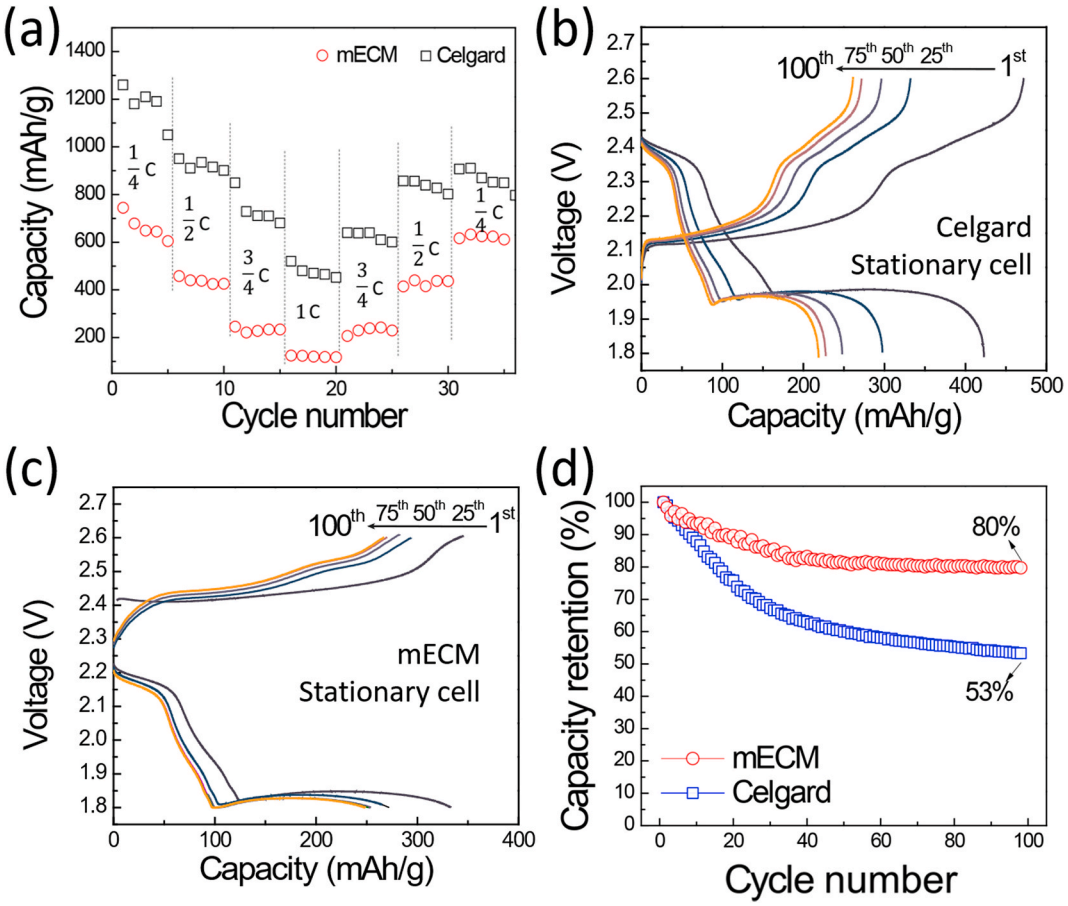

Fig. 4. (a) C-rate performance of the Li-PS cell with the mECM and Celgard 2325. (b) Charge–discharge profiles (1.8–2.6 V) of the nonflowing Li-PS cell with Celgard 2325 at a rate of 0.75C from the 1st to 100th cycle. (c) Charge–discharge profiles (1.8–2.6 V) of the nonflowing Li-PS cell with the mECM at a rate of 0.75C from the 1st to 100th cycle. (d) Capacity retention curves of the nonflowing Li-PS cell with Celgard 2325 and the mECM at a rate of 0.75C.

Celgard 2325 via a series of galvanostatic charging and discharging steps at rates of 0.25–1 C with a potential window of 1.8–2.6 V. As shown in Fig. 4a, Celgard 2325 shows higher capacity values than mECM due to its lower membrane resistance. However, its battery capacity quickly decays at all C-rates. In comparison, mECM shows a better stability on the rate-performance. Although the capacity decay rate of mECM decreases at high C-rates, the total capacity also decreases because of the high overpotential at the elevated current. From these results, we chose to measure the cycle stability at an intermediate C-rate (0.75C), at which our batteries can maintain a high capacity. Then, we evaluated the cycle stability of the mECM in a stationary cell. For comparison, a reference cell assembled with Celgard 2325 was operated under the same condition. Notably, we were not able to charge and discharge the cell with Nafion117 due to its poor selectivity and significant swelling in the organic electrolyte. Fig. 4b and c shows charge–discharge curves of Celgard 2325 and the mECM at a rate of 0.75C with a potential window of 1.8–2.6 V. All charge–discharge curves exhibit two typical discharge plateaus near 2.3 and 2.1 V, corresponding to the reduction processes of $S_8 \rightarrow Li_2S_n$ ($4 \leq n \leq 6$) and Li_2S_n ($4 \leq n \leq 6$) $\rightarrow Li_2S_n$ ($1 \leq n \leq 2$), respectively. The Li-PS cell with the mECM shows a higher overpotential for both charging and discharging than the cell with Celgard 2325 because of its higher membrane resistance. However, the capacity of the Li-PS static cell with the Celgard separator decreases more rapidly than that of the mECM, as evidenced in the charge–discharge curves for different cycle numbers. Next, we evaluated the cycle stability of the mECM and Celgard 2325 using the stationary cell at a rate of 0.75C. As exhibited in Fig. 4d, the Li-PS stationary cell with the mECM retains a high capacity (>80% of original) after 100 cycles of the charge–discharge test. In particular, the capacity of the Li-PS cell with the mECM reaches a plateau at 40 cycles. In contrast, the Li-PS static cell with Celgard 2325 shows a rapid capacity decay, and the capacity decreases to 50% at 100 cycles. This result indicates that the mECM achieves excellent stability in the Li-PS cell by effectively suppressing the PS shuttling effect, rendering the mECM more promising for long-term operation than the porous Celgard separator.

As the mECM has exhibited outstanding electrochemical characteristics and stable cycling performance with stationary cells, we further evaluated its performance using a Li-PS RFB cell (Fig. 5a). A charge–discharge test was conducted on the RFB cell with the mECM and Celgard 2325 at a current of 0.75C. To minimize the deposition of insoluble short-chain PS species (i.e., Li_2S_n, $1 \leq n \leq 2$) on the surface of the carbon electrode and membrane during charge-discharge period longer than the static-cell test when a large volume of electrolyte is used, we tested the flow cell with a narrower voltage window of 1.9–2.6 V, instead of the voltage window of 1.8–2.6 V used in the static cell test. As shown in the charge–discharge curves (Fig. 5b), the flow cell with Celgard 2325 starts with a capacity of 354 mAh/g in the first cycle. However, its capacity rapidly decreases over the test and reaches a much lower value of 27 mAh/g at 25 cycles. In comparison, although the cell with the mECM exhibits a lower initial capacity (142 mAh/g), its decay rate is significantly lower than that of Celgard 2325, which is largely attributed to the excellent ability of the mECM to suppress PS crossover (Fig. 5c). Of note, the capacity of the Li-PS RFB with the mECM (~140 mAh/g) is still higher than that of VRFBs (10–20 mAh/g) by an order of magnitude. At 100 cycles of the charge–discharge test, the cell with Celgard 2325 lost 67% of its initial capacity (33% capacity retention and 0.33% decay per cycle); in contrast, the flow cell with the mECM maintained a high capacity of 78% (Fig. 5d and Fig. S6), demonstrating the ability of our mECM to ensure reliable performance in Li-PS batteries for long-term operation. Moreover, after the capacity of the RFB cell

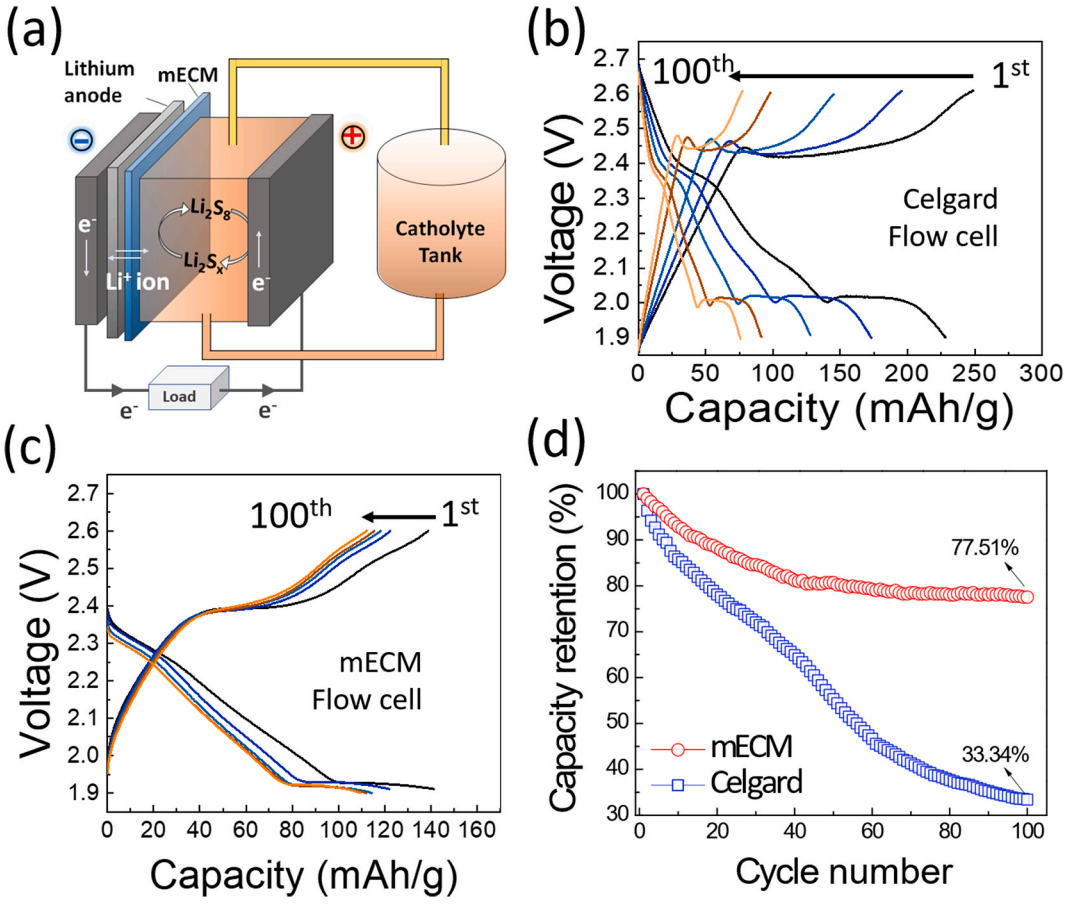

Fig. 5. (a) Schematic illustration of Li-PS RFB cell. Charge–discharge profiles (1.9–2.6 V) of the Li-PS RFB cell with (b) Celgard 2325 and (c) mECM at a rate of 0.75C from the 1st to 100th cycle. (d) Capacity retention curves of the Li-PS RFB cell with Celgard 2325 and the mECM at a rate of 0.75C.

with the mECM reaches a plateau at 40 cycles, similar to the static cell (Fig. 4d), the capacity of the mECM decreases only 3% over a subsequent 60 cycles (0.05% decay per cycle). In addition, the flow cell with the Celgard separator shows unstable and low coulombic efficiency (Fig. S7). Meanwhile, the RFB cell with the mECM maintains a high coulombic efficiency (close to 100%), voltage efficiency (96%), and energy efficiency (96%) during the entire cycle, even in the absence of a $LiNO_3$ anode-protecting additive (Fig. S8), which suggests efficient suppression of PS ion shuttling by our mECM. It is worth mentioning that a low Li-PS concentration (0.1 M) in DOL/DME was used in this study to demonstrate the PS-blocking characteristics of the mECM, which can minimize the effect of solid precipitation of the insoluble short-chain PS formed during long-term cycling tests [46]. To improve the solubility of Li-PS in organic solvent and to enhance the volumetric capacity of the cell, our future work will focus on employing organic solvents with a higher dielectric constant (e.g., dimethyl sulfoxide, tetrahydrofuran), which can increase the PS concentration up to 3 M and suppress the formation of insoluble short-chain Li-PS species [46]. Moreover, in future work, we will explore the optimization of operating parameters for the Li-PS RFB cell, such as the type and concentration of supporting electrolyte, electrolyte viscosity, flow rate, carbon electrodes, membrane thickness, flow channel dimensions, current density, and voltage window.

4. Conclusions

In this work, we developed a novel mECM with a unique bilayer structure consisting of a highly lithium-ion-selective ion exchange polymer, a porous CNT layer, and a BNNT support layer for the application of Li-PS RFBs. The BPSA ion exchange polymer, which has excellent chemical resistance in organic solvent, plays a critical role in blocking the transport of PS active species while allowing Li^+ ion conduction. The highly entangled CNT buckypaper not only greatly enhances the dimensional stability of the ion exchange polymer in the DOL/DME electrolyte but also effectively reduces the interfacial resistance between the membrane and electrode. The non-electrically-conductive BNNT layer facing the lithium anode facilitates heat dissipation and suppresses lithium dendrite growth. Consequently, the mECM exhibits a much higher Li^+/PS ion selectivity than a commercial polyolefin separator (i.e., Celgard 2325) and CEM (i.e., Nafion) and can be considered as a more promising separator for Li-PS RFBs. Li-PS cells equipped with the mECM exhibited stable electrochemical performance over 100 cycles at 0.75C, with a capacity retention close to 80%. In contrast, the reference cell with Celgard 2325, a commonly used porous battery separator, showed a much higher capacity decay rate and almost fully lost its capacity, with only 3% capacity retention at 40 cycles. Our work emphasizes the critical role of chemically stable, highly ion-selective membranes for high-energy-density organic RFBs and provides a feasible strategy of using multifunctional membranes to enhance the electrochemical performance of Li-PS batteries.

Author statement

Tongshuai Wang: Investigation, Formal analysis, Writing- Original Draft. Xiaofeng Wang: Investigation. Aaditya Pendse: Investigation. Yuechen Gao: Investigation. Kun Wang: Investigation. Chulsung Bae: Supervision, Writing-Review & Editing. Sangil Kim: Conceptualization, Supervision, Writing-Review & Editing.

Declaration of competing interest

The authors declare that they have no known competing financial interests or personal relationships that could have appeared to influence the work reported in this paper.

Acknowledgements

This work was supported by grants from the National Science Foundation (Grant No. CBET-1706910), the U.S. Department of Energy, Small Business Technology Transfer (DOE/STTR; Award No. 242675), and the New York State Energy Research and Development Authority (NYSERDA; Grant No. 127734). T. Wang acknowledges support from the UIC Provost's Graduate Research Award program. S. Kim and C. Bae thank Xergy Inc. for discussions.

Appendix A. Supplementary data

Supplementary data to this article can be found online at https://doi.org/10.1016/j.memsci.2021.119539.

References

[1] N. Li, Z. Weng, Y. Wang, F. Li, H.-M. Cheng, H. Zhou, An aqueous dissolved polysulfide cathode for lithium–sulfur batteries, Energy Environ. Sci. 7 (2014) 3307–3312.
[2] D. Bresser, S. Passerini, B. Scrosati, Recent progress and remaining challenges in sulfur-based lithium secondary batteries–a review, Chem. Commun. 49 (2013) 10545–10562.
[3] J. Sun, Y. Sun, M. Pasta, G. Zhou, Y. Li, W. Liu, F. Xiong, Y. Cui, Entrapment of polysulfides by a black-phosphorus-modified separator for lithium–sulfur batteries, Adv. Mater. 28 (2016) 9797–9803.
[4] A. Manthiram, An outlook on lithium ion battery technology, ACS Cent. Sci. 3 (2017) 1063–1069.
[5] G. Zubi, R. Dufo-López, M. Carvalho, G. Pasaoglu, The lithium-ion battery: state of the art and future perspectives, Renew. Sustain. Energy Rev. 89 (2018) 292–308.
[6] D. Chen, M.A. Hickner, E. Agar, E.C. Kumbur, Optimized anion exchange membranes for vanadium redox flow batteries, ACS Appl. Mater. Interfaces 5 (2013) 7559–7566.
[7] M. Rychcik, M. Skyllas-Kazacos, Characteristics of a new all-vanadium redox flow battery, J. Power Sources 22 (1988) 59–67.
[8] W. Wang, Q. Luo, B. Li, X. Wei, L. Li, Z. Yang, Recent progress in redox flow battery research and development, Adv. Funct. Mater. 23 (2013) 970–986.
[9] F. Pan, Q. Huang, H. Huang, Q. Wang, High-energy density redox flow lithium battery with unprecedented voltage efficiency, Chem. Mater. 28 (2016) 2052–2057.
[10] L. Zhang, Q. Lai, J. Zhang, H. Zhang, A high-energy-density redox flow battery based on zinc/polyhalide chemistry, ChemSusChem 5 (2012) 867–869.
[11] A. Manthiram, Y. Fu, S.-H. Chung, C. Zu, Y.-S. Su, Rechargeable lithium–sulfur batteries, Chem. Rev. 114 (2014) 11751–11787.
[12] X. Zhou, T. Zhao, L. An, Y. Zeng, L. Wei, Critical transport issues for improving the performance of aqueous redox flow batteries, J. Power Sources 339 (2017) 1–12.
[13] Z.W. Seh, Y. Sun, Q. Zhang, Y. Cui, Designing high-energy lithium–sulfur batteries, Chem. Soc. Rev. 45 (2016) 5605–5634.
[14] L. Qie, C. Zu, A. Manthiram, A high energy lithium-sulfur battery with ultrahigh-loading lithium polysulfide cathode and its failure mechanism, Adv. Energy Mater. 6 (2016) 1502459.
[15] A. Fotouhi, D.J. Auger, L. O'Neill, T. Cleaver, S. Walus, Lithium-sulfur battery technology readiness and applications—a review, Energies 10 (2017) 1937.
[16] K. Dong, S. Wang, J. Yu, A lithium/polysulfide semi-solid rechargeable flow battery with high output performance, RSC Adv. 4 (2014) 47517–47520.
[17] Y. Yang, G. Zheng, Y. Cui, A membrane-free lithium/polysulfide semi-liquid battery for large-scale energy storage, Energy Environ. Sci. 6 (2013) 1552–1558.
[18] H. Chen, G. Cong, Y.-C. Lu, Recent progress in organic redox flow batteries: active materials, electrolytes and membranes, Journal of Energy Chemistry 27 (2018) 1304–1325.
[19] C. Li, A.L. Ward, S.E. Doris, T.A. Pascal, D. Prendergast, B.A. Helms, Polysulfide-blocking microporous polymer membrane tailored for hybrid Li-sulfur flow batteries, Nano Lett. 15 (2015) 5724–5729.
[20] J.-Q. Huang, T.-Z. Zhuang, Q. Zhang, H.-J. Peng, C.-M. Chen, F. Wei, Permselective graphene oxide membrane for highly stable and anti-self-discharge lithium–sulfur batteries, ACS Nano 9 (2015) 3002–3011.
[21] J.-Q. Huang, Q. Zhang, H.-J. Peng, X.-Y. Liu, W.-Z. Qian, F. Wei, Ionic shield for polysulfides towards highly-stable lithium–sulfur batteries, Energy Environ. Sci. 7 (2014) 347–353.
[22] S. Bai, X. Liu, K. Zhu, S. Wu, H. Zhou, Metal–organic framework-based separator for lithium–sulfur batteries, Nat. Energy 1 (2016) 1–6.
[23] J.-Q. Huang, Q. Zhang, F. Wei, Multi-functional separator/interlayer system for high-stable lithium-sulfur batteries: progress and prospects, Energy Storage Mater 1 (2015) 127–145.
[24] W. Kou, X. Li, Y. Liu, X. Zhang, S. Yang, X. Jiang, G. He, Y. Dai, W. Zheng, G. Yu, Triple-layered carbon-SiO2 composite membrane for high energy density and long cycling Li–S batteries, ACS Nano 13 (2019) 5900–5909.
[25] Z.A. Ghazi, X. He, A.M. Khattak, N.A. Khan, B. Liang, A. Iqbal, J. Wang, H. Sin, L. Li, Z. Tang, MoS2/celgard separator as efficient polysulfide barrier for long-life lithium–sulfur batteries, Adv. Mater. 29 (2017) 1606817.

[26] D. Aaron, Q. Liu, Z. Tang, G. Grim, A. Papandrew, A. Turhan, T. Zawodzinski, M. Mench, Dramatic performance gains in vanadium redox flow batteries through modified cell architecture, J. Power Sources 206 (2012) 450–453.
[27] X. Li, H. Zhang, Z. Mai, H. Zhang, I. Vankelecom, Ion exchange membranes for vanadium redox flow battery (VRB) applications, Energy Environ. Sci. 4 (2011) 1147–1160.
[28] H. Prifti, A. Parasuraman, S. Winardi, T.M. Lim, M. Skyllas-Kazacos, Membranes for redox flow battery applications, Membranes 2 (2012) 275–306.
[29] T. Wang, J.Y. Jeon, J. Han, J.H. Kim, C. Bae, S. Kim, Poly (terphenylene) anion exchange membranes with high conductivity and low vanadium permeability for vanadium redox flow batteries (VRFBs), J. Membr. Sci. 598 (2020) 117665.
[30] X. Yu, S. Feng, M.J. Boyer, M. Lee, R.C. Ferrier Jr., N.A. Lynd, G.S. Hwang, G. Wang, S. Swinnea, A. Manthiram, Controlling the polysulfide diffusion in lithium-sulfur batteries with a polymer membrane with intrinsic nanoporosity, Mater. Today Energy 7 (2018) 98–104.
[31] X. Cheng, W. Wang, A. Wang, K. Yuan, Z. Jin, Y. Yang, X. Zhao, Oxidized multiwall carbon nanotube modified separator for high performance lithium–sulfur batteries with high sulfur loading, RSC Adv. 6 (2016) 89972–89978.
[32] Q. Xu, G. Hu, H. Bi, H. Xiang, A trilayer carbon nanotube/Al 2 O 3/polypropylene separator for lithium-sulfur batteries, Ionics 21 (2015) 981–986.
[33] L. Tan, X. Li, Z. Wang, H. Guo, J. Wang, L. An, Multifunctional separator with porous carbon/multi-walled carbon nanotube coating for advanced Lithium–sulfur batteries, ChemElectroChem 5 (2018) 71–77.
[34] Y. Fan, D. Liu, M.M. Rahman, T. Tao, W. Lei, S. Mateti, B. Yu, J. Wang, C. Yang, Y. Chen, Repelling polysulfide ions by boron nitride nanosheet coated separators in lithium–sulfur batteries, ACS Appl. Energy Mater. 2 (2019) 2620–2628.
[35] G.S. McKee, C.P. Deck, K.S. Vecchio, Dimensional control of multi-walled carbon nanotubes in floating-catalyst CVD synthesis, Carbon 47 (2009) 2085–2094.
[36] T. Wang, J. Han, K. Kim, A. Münchinger, Y. Gao, A. Farchi, Y.-K. Choe, K.-D. Kreuer, C. Bae, S. Kim, Suppressing vanadium crossover using sulfonated aromatic ion exchange membranes for high performance flow batteries, Materials Advances 1 (2020) 2206–2218.
[37] W.-H. Lee, E.J. Park, J. Han, D.W. Shin, Y.S. Kim, C. Bae, Poly (terphenylene) anion exchange membranes: the effect of backbone structure on morphology and membrane property, ACS Macro Lett. 6 (2017) 566–570.
[38] M.K. Pagels, S. Adhikari, R.C. Walgama, A. Singh, J. Han, D. Shin, C. Bae, One-pot synthesis of proton exchange membranes from anion exchange membrane precursors, ACS Macro Lett. 9 (2020) 1489–1493.
[39] T. Wang, J.Y. Jeon, J. Han, J.H. Kim, C. Bae, S. Kim, Poly(terphenylene) anion exchange membranes with high conductivity and low vanadium permeability for vanadium redox flow batteries (VRFBs), J. Membr. Sci. 598 (2020) 117665.
[40] T. Wang, S.J. Moon, D.-S. Hwang, H. Park, J. Lee, S. Kim, Y.M. Lee, S. Kim, Selective ion transport for a vanadium redox flow battery (VRFB) in nano-crack regulated proton exchange membranes, J. Membr. Sci. 583 (2019) 16–22.
[41] R. Arenal, A. Ferrari, S. Reich, L. Wirtz, J.-Y. Mevellec, S. Lefrant, A. Rubio, A. Loiseau, Raman spectroscopy of single-wall boron nitride nanotubes, Nano Lett. 6 (2006) 1812–1816.
[42] S. Saha, D. Muthu, D. Golberg, C. Tang, C. Zhi, Y. Bando, A. Sood, Comparative high pressure Raman study of boron nitride nanotubes and hexagonal boron nitride, Chem. Phys. Lett. 421 (2006) 86–90.
[43] S. Sakurai, F. Kamada, D.N. Futaba, M. Yumura, K. Hata, Influence of lengths of millimeter-scale single-walled carbon nanotube on electrical and mechanical properties of buckypaper, Nanoscale Res. Lett. 8 (2013) 1–7.
[44] D.-H. Kim, H.-K. Jang, M.-S. Kim, S.-D. Kim, D.-J. Lee, G.T. Kim, Conductive multi-walled boron nitride nanotubes by catalytic etching using cobalt oxide, Phys. Chem. Chem. Phys. 19 (2017) 976–985.
[45] Z. Sun, X.L. Wu, Z. Peng, J. Wang, S. Gan, Y. Zhang, D. Han, L. Niu, Compactly coupled nitrogen-doped carbon nanosheets/molybdenum phosphide nanocrystal hollow nanospheres as polysulfide reservoirs for high-performance lithium–sulfur chemistry, Small 15 (2019) 1902491.
[46] H. Pan, X. Wei, W.A. Henderson, Y. Shao, J. Chen, P. Bhattacharya, J. Xiao, J. Liu, On the way toward understanding solution chemistry of lithium polysulfides for high energy Li–S redox flow batteries, Advanced Energy Materials 5 (2015) 1500113.